small methods
www.small-methods.com

Degradation and Self-Healing of $FAPbBr_3$ Perovskite under Soft-X-Ray Irradiation

Valeria Milotti, Stefania Cacovich, Davide Raffaele Ceratti, Daniel Ory, Jessica Barichello, Fabio Matteocci, Aldo Di Carlo, Polina M. Sheverdyaeva, Philip Schulz,* and Paolo Moras**

The extensive use of perovskites as light absorbers calls for a deeper understanding of the interaction of these materials with light. Here, the evolution of the chemical and optoelectronic properties of formamidinium lead tri-bromide ($FAPbBr_3$) films is tracked under the soft X-ray beam of a high-brilliance synchrotron source by photoemission spectroscopy and micro-photoluminescence. Two contrasting processes are at play during the irradiation. The degradation of the material manifests with the formation of Pb^0 metallic clusters, loss of gaseous Br_2, decrease and shift of the photoluminescence emission. The recovery of the photoluminescence signal for prolonged beam exposure times is ascribed to self-healing of $FAPbBr_3$, thanks to the re-oxidation of Pb^0 and migration of FA^+ and Br^- ions. This scenario is validated on $FAPbBr_3$ films treated by Ar^+ ion sputtering. The degradation/self-healing effect, which is previously reported for irradiation up to the ultraviolet regime, has the potential of extending the lifetime of X-ray detectors based on perovskites.

1. Introduction

Hybrid organic inorganic metal tri-halide perovskites are attracting growing interest for photonic applications, as their optoelectronic properties can be easily tailored by tuning their chemical composition.[1–3] Potential fields of use include photovoltaics, thanks to power conversion efficiencies close to those of monocrystalline silicon solar cells,[4–6] and ionizing radiation detection for space applications or medical imaging. [7–9] Studying the effects of light irradiation on these materials over a wide spectral range is of crucial importance, in order to determine, for instance, the mechanisms of deterioration of device performances.

Hybrid organic inorganic lead tri-halide perovskites are represented by the formula $APbX_3$, where site A is filled by an organic cation (such as methylammonium or formamidinium $FA^+ = CH(NH_2)_2^+$) and site X by halides.[10] A relevant property of solar cells based on $APbX_3$ perovskites is the extended working lifetime, as a result of self-healing processes occurring within the perovskite layers.[11–13] In fact, the quality of the perovskites, which is degraded by external stressors, such as light exposure, tends to recover automatically when the stressor is removed.[14–18] These processes originate from the low activation energies of chemical reactions and migration of

V. Milotti[+], P. M. Sheverdyaeva, P. Moras
Istituto di Struttura della Materia - CNR (ISM-CNR)
Trieste I-34149, Italy
E-mail: valeria.milotti@unipd.it; paolo.moras@trieste.ism.cnr.it
S. Cacovich, D. R. Ceratti, P. Schulz
Institut Photovoltaïque d'Île de France (IPVF)
CNRS, Ecole Polytechnique, IP Paris
Palaiseau 91120, France
E-mail: philip.schulz@cnrs.fr

The ORCID identification number(s) for the author(s) of this article can be found under https://doi.org/10.1002/smtd.202300222

[+]Present address: Department of Physics and Astronomy, University of Padua, Padua 35121, Italy

DOI: 10.1002/smtd.202300222

D. R. Ceratti
Sorbonne Université
CNRS, Collège de France
UMR 7574, Chimie de la Matière Condensée de Paris,
Paris 75005, France
D. Ory
Institut Photovoltaïque d'Île-de-France (IPVF)
18 Boulevard Thomas Gobert
Palaiseau 91120, France
D. Ory
Électricité de France (EDF), R&D
18 Boulevard Thomas Gobert
Palaiseau 91120, France
J. Barichello, F. Matteocci, A. Di Carlo
CHOSE (Centre for Hybrid and Organic Solar Energy)
Department of Electronic Engineering
University of Rome "Tor Vergata,"
Rome 00133, Italy
A. Di Carlo
Istituto di Struttura della Materia - CNR (ISM-CNR)
Rome 00133, Italy

ionic species in $APbX_3$ perovskites.[19–27] Anions are the most mobile species, while Pb^{2+} is found to be the slowest moving species.[28,29]

$APbX_3$ perovskites incorporating FA^+ and Br^- ions display higher stability than other compositions under external stresses.[30–36] For this reason, $FAPbBr_3$ has been used as an active layer for both rigid and flexible solar cells.[37–39] Owing to its large bandgap (2.2 eV), $FAPbBr_3$ has been considered as one of the best photo-active material for semitransparent solar cell for Building Integrated Photovoltaics.[39–41] $FAPbBr_3$ nanocrystals are used in the active layer of light-emitting diodes.[42] The resistance of $FAPbBr_3$ to high temperatures and irradiation makes it a good candidate also for X-ray detectors and space applications.[43–47]

The present study focuses on the chemical and optoelectronic properties of $FAPbBr_3$ films under soft X-ray irradiation. High-brilliance synchrotron light is employed to accelerate the ageing of the material. X-ray photoemission spectroscopy (XPS) shows the formation of Pb^0 metallic clusters and loss of gaseous Br_2, which are distinctive fingerprints of degradation of the perovskite. The observed rate of decomposition suggests the existence of a counterbalancing process. Micro-photoluminescence (PL) spectroscopy reveals that soft X-ray irradiation has different effects on $FAPbBr_3$ depending on the exposure conditions. The degradation occurring at low photon density irradiation is followed by self-healing of the material at higher photon density, owing to the re-oxidation of Pb^0 and the mobility of the FA^+ and Br^- ions. This scenario is confirmed on Ar^+ ion sputtered $FAPbBr_3$ films, which display different degradation and self-healing rates with respect to the pristine case. The present results complement similar observations on $FAPbBr_3$ films irradiated with lower photon energies[14,21] and pave the way toward advanced applications of this material in the field of X-ray detection.

2. Results and Discussion

High-quality $FAPbBr_3$ is synthesized according to well-established procedures[48] and deposited on conductive substrates in the form of films with thickness of about 350 nm. Irradiation and XPS experiments are performed at photon energy $h\nu = 750$ eV, with an average flux of 10^{10} photons per second. Almost 99% of the photon flux is concentrated in an oval spot of about 250 μm × 400 μm (7.9×10^4 μm^2). The remaining 1% of stray light, which derives from the non-ideal alignment of the beamline optical elements, is spread over a wider region of low photon density surrounding the oval spot. While the penetration depth of the soft X-rays (> 1 mm) is larger than the film thickness, the XPS signal originates from a region close to the film surface, due to the short inelastic mean free path of electrons with kinetic energies below 750 eV (1–2 nm). As shown in the following, the combination of surface-sensitive XPS and bulk-sensitive PL measurements is suitable to understand the effects of X-ray irradiation on $FAPbBr_3$. The experimental results are presented in Sections 2.1 and 2.2 for pristine and sputtered $FAPbBr_3$ films, respectively. The optoelectronic properties of the two systems are compared in Section 2.3.

2.1. Irradiation of Pristine $FAPbBr_3$ Films

XPS spectra are collected on the same position of the sample at intervals of 14 min (5 sets of spectra in 70 min) in order to characterize the changes of the surface chemical properties of $FAPbBr_3$ as a function of the irradiation time. All expected elements are detected in the survey spectrum of **Figure 1**a,[37,42] including oxygen deriving from air exposure. Figure 1b–e compares the relevant core level lines of $FAPbBr_3$ corresponding to the first and last set of spectra. In the N 1s region (Figure 1b) the single peak observed at 400.5 eV (N in FA^+) broadens by 13% (full width at half maximum, FWHM) and is accompanied by another peak at 399.3 eV after prolonged irradiation. We attribute the additional peak at lower binding energy to decomposition products of FA^+. While the complex decomposition process of formamidinium is still under debate,[49] sym-triazine and hydrogen cynanide have been identified after film degradation and accelerated ageing.[35] Here, the formation of the new peak in the XPS data is consistent with the binding energy for nitrogen coordinated in an azine group. Two C 1s peaks (Figure 1c) are associated to C in FA^+ (288.3 eV), for which we observe a broadening of 15% (FWHM) after prolonged irradiation, and surface contamination by adventitious C (284.7 eV). The drop of the latter peak as a function of the irradiation time, probably due to light-stimulated release of C from the surface, explains the overall increase of the signal of $FAPbBr_3$-related peaks. The broadening of the N 1s and C 1s peaks indicates changes in the immediate chemical environment of FA^+, for instance due to the creation of defects such as vacancies of Pb and/or Br on neighboring crystallographic sites, which will be discussed in the quantitative analysis of the atomic ratios later in the paper. The main Pb 4f doublet (Figure 1d), corresponding to Pb^{2+} in the perovskite, shows a shift toward higher binding energies for prolonged irradiation (from 138.7 to 138.9 eV for the $4f_{7/2}$ component), while another much weaker Pb 4f doublet emerges at lower binding energies ($4f_{7/2}$ component at 136.8 eV). Also Br 3d (Figure 1e) presents a shift toward higher binding energies as a function of irradiation time (from 68.5 to 68.7 eV for the $3d_{5/2}$ component).

All these experimental observations can be rationalized by considering the photo-degradation path of $APbX_3$ perovskites, which consists of two main steps. In the first step $APbX_3 \rightarrow PbX_2 + AX$, that is, for the specific case of $FAPbBr_3$:[14]

$$FAPbBr_3 \longleftrightarrow PbBr_2 + FABr \quad (1)$$

$PbBr_2$ further degrades into:

$$PbBr_2 \rightarrow Pb^0 + Br_2\ (g) \quad (2)$$

thus making Br_2 gas and Pb^0, metallic lead, characteristic side-products of the decomposition.[50,51] Notably, this process is analogous to the decomposition of PbI_2, which has been used as a photo-sensitive material in photography because it easily decomposes to metallic lead under illumination.[52]

The second Pb 4f doublet emerging in Figure 1d under irradiation is thus associated to the formation of Pb^0, most probably agglomerated in metallic clusters, on the film surface.[50,53] Its evolution can be better seen in **Figure 2**a, where the Pb $4f_{7/2}$ components of Pb^{2+} and Pb^0 are displayed as a function of the

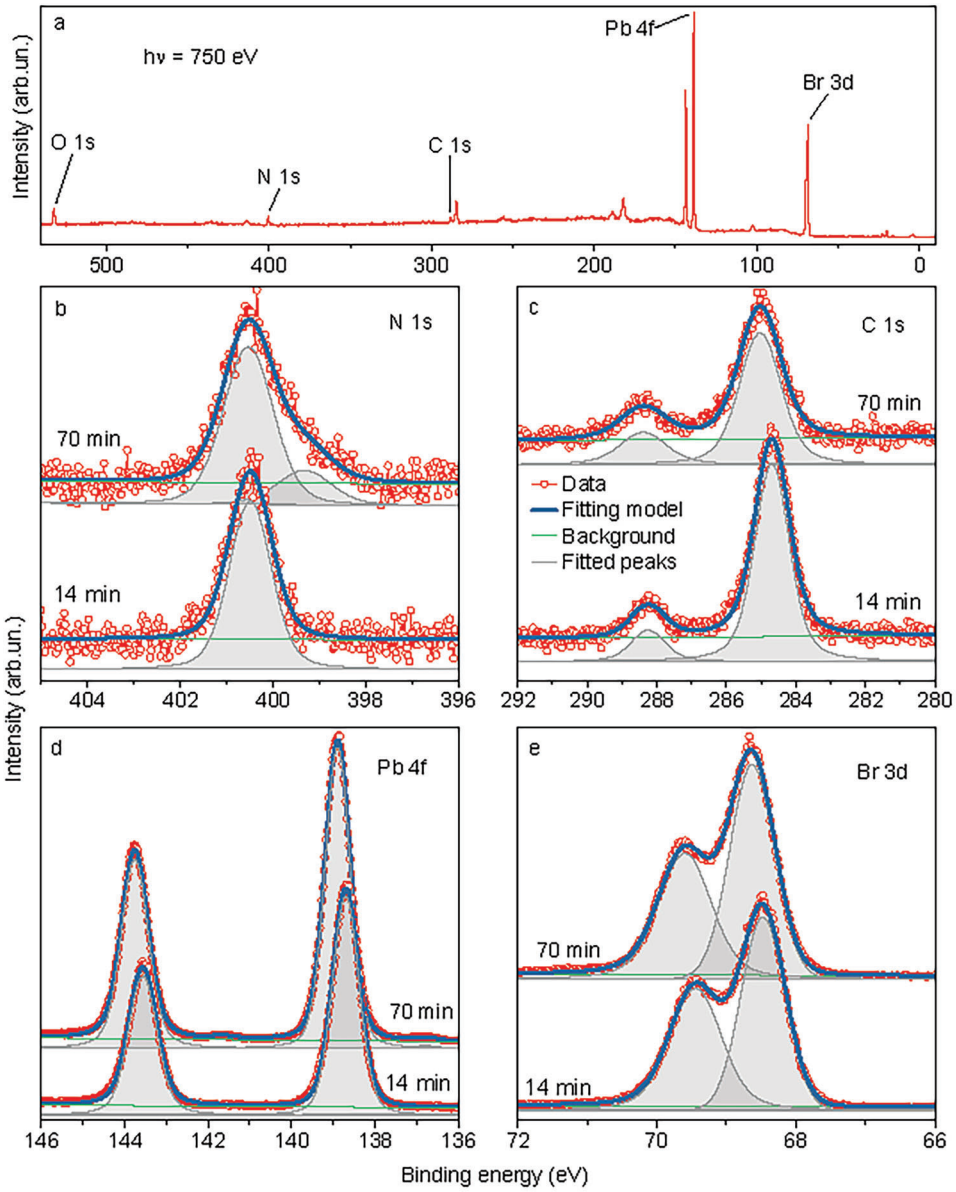

Figure 1. XPS data of pristine $FAPbBr_3$. a) Survey spectrum. b–e) Core level spectra extracted from the first (14 min) and last (70 min) sets of data and related fittings: (b) N 1s, (c) C 1s, (d) Pb 4f, and (e) Br 3d.

irradiation time. Metallic Pb^0 clusters act as donor defects and cause Fermi level pinning close to the bottom of the conduction band of $FAPbBr_3$.[54,55] This explains the downward shift of the core level lines.

For a quantitative analysis of the XPS data it is useful to compare the experimental atomic ratios referred to the total lead content $Pb^{tot} = Pb^{2+} + Pb^0$ (Figure 2b, see Experimental Section for the derivation) to those expected from the chemical formula of $FAPbBr_3$, that is, $Br/Pb^{tot} = 3$, $N/Pb^{tot} = 2$ and $C/Pb^{tot} = 1$. The first experimental value of Br/Pb^{tot} is 2.95 and shows that Br is nearly stoichiometric in the film surface, while N (N/Pb^{tot} = 0.42) and C (C/Pb^{tot} = 0.36) are significantly understoichiometric. This discrepancy can be attributed to vacuum degassing of FA^+ from the film surface, as it will be pointed out in Section 2.2.

Importantly, Br/Pb^{tot} decreases from 2.95 to 2.4 (-18.6 %) after 70 min irradiation, while N/Pb^{tot} and C/Pb^{tot} remain approximately constant. This suggests that gaseous Br_2 produced by reaction (2) is released from the film surface. However, the decrease of Br/Pb^{tot} turns out to be much larger than the formation of Pb^0 (Pb^0/Pb^{tot} = 0.01 for 70 min irradiation, inset of Figure 2a). This is an indication that Pb^0 is partially re-oxidized to Pb^{2+} through the reaction:

$$Pb^0 + 2H^+ \rightarrow Pb^{2+} + H_2\,(g) \quad (3)$$

The re-oxidation of Pb^0 by an acid is a thermodynamically favored reaction. Moreover, as molecular hydrogen leaves the sample, the reaction proceeds favorably also thanks to the law of mass action.

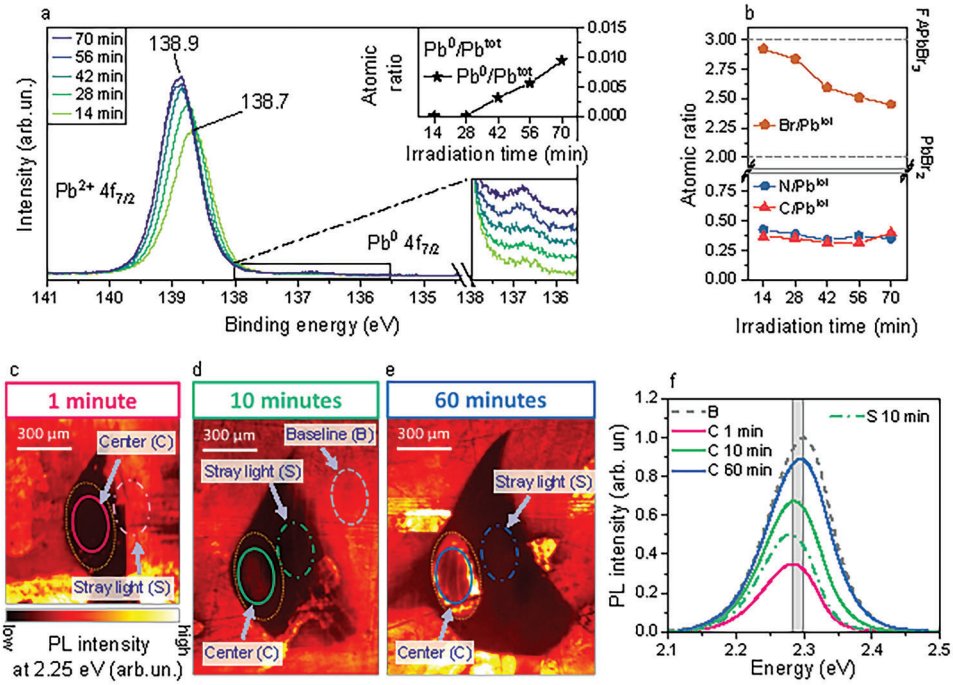

Figure 2. a) Pb $4f_{7/2}$ spectra of pristine $FAPbBr_3$: the main peak is ascribed to Pb^{2+}, the smaller feature to Pb^0 (zoom in the bottom inset). The Pb^0/Pb^{tot} atomic ratio is shown in the top inset. b) Br/Pb^{tot}, N/Pb^{tot}, and C/Pb^{tot} atomic ratios for pristine $FAPbBr_3$. Dashed lines indicate the expected Br/Pb^{tot} ratio in pristine $FAPbBr_3$ and $PbBr_2$. c–e) PL maps at 2.25 eV after (c) 1, (d) 10, and (e) 60 min irradiation. The same scale and contrast bars apply to all images. Yellow dotted lines enclose the high photon flux spot of synchrotron light. f) PL spectra collected in the areas indicated by ovals in (c–e). Dashed, continuous, and dash-dotted lines are used for the baseline (B), center (C), and stray light (S) spectra. The shaded rectangle highlights the shift of the PL emission.

The presence of Pb^{2+} opens a pathway for self-healing at the surface that circumvents the loss of gaseous Br_2. FA^+ is the conjugated acid of formamidine ($HC(NH_2)NH$), which can form bonds with Pb^{2+}, thus stabilizing its deprotonated form and increasing its acidity. This process is described by the reaction (structural form in Figure S2, Supporting Information):

$$FA^+ + Pb^{2+} \rightleftharpoons HC(NH_2)NH - Pb^{2+} + H^+ \quad (4)$$

Reactions (3) and (4) together give:

$$2FA^+ + 2Pb^0 \longrightarrow 2HC(NH_2)NH - Pb^{2+} + H_2\ (g) \quad (5)$$

where each $HC(NH_2)NH$-Pb^{2+} can be seen as a vacancy of H^+ inside $FAPbBr_3$.[21,22] As the addition of methylamine to methylammonium-based perovskites has been shown to improve their quality,[56] an equivalent improvement in degraded $FAPbBr_3$ is expected once formamidine is formed through reaction (5). Of course, complete self-healing of $FAPbBr_3$ is disfavored at the surface due to the loss of gaseous Br_2 but can occur in the bulk, as the following PL data demonstrate.

The effects of X-ray irradiation on the optoelectronic properties of the $FAPbBr_3$ films are investigated by using PL imaging analysis.[57,58] Spectrally resolved multidimensional datasets (x, y, λ) are acquired on samples exposed to the synchrotron beam for 1, 10, and 60 min. Figure 2c–e reports the corresponding PL maps at $h\nu = 2.25$ eV.

As we anticipated at the beginning of this section, 99% of the X-ray flux is concentrated within the spot delimited by the yellow dotted lines (Figure 2c–e). In this area, the PL signal is low for 1 min irradiation (Figure 2c) and increases with increasing the irradiation time (Figure 2d,e). This behavior is a clear signature of the self-healing effect occurring in the bulk of the $FAPbBr_3$ film between 1 and 10 min irradiation. It can be described by examining the PL spectra of Figure 2f, which are extracted from the ovals with area 6×10^4 μm^2 indicated in Figure 2c–e. The gray dashed line represents the reference baseline (B) spectrum acquired away from the region irradiated by X-rays, with maximum at 2.299 eV. The spectra acquired at the center (C) of the X-ray spot show that the PL emission for 1 min irradiation (pink continuous line) is much less intense (33%) and red-shifted (2.282 eV) with respect to spectrum B. Both intensity and peak position of spectra C for 10 (green continuous line) and 60 min (blue continuous line) tend to approach those of spectrum B. In particular, for 60 min irradiation the intensity reaches 88% of spectrum B and the peak maximum is located at 2.295 eV.

The high flux spot enclosed by the yellow dotted line in Figure 2c–e is surrounded by areas of low PL intensity and irregular shape, which extend laterally with increasing the irradiation time. These areas receive stray light, corresponding to 1% of the total photon flux. Their evolution gives us the opportunity to follow the initial degradation process of $FAPbBr_3$. The PL spectrum collected in the oval labeled S in Figure 2d (green dash-dotted line) has 50% of the intensity of spectrum B and peak maximum at 2.275 eV. Instead, most of the same area in Figure 2c looks

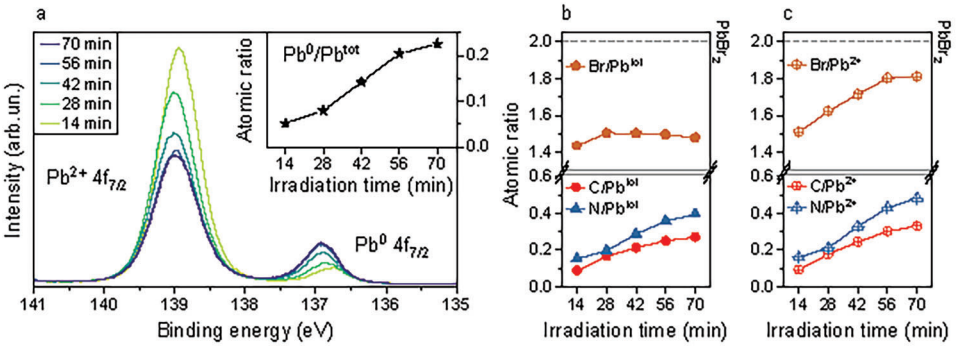

Figure 3. a) Pb $4f_{7/2}$ spectra of the 6 min sputtered $FAPbBr_3$ film under irradiation: left and right peaks are ascribed to Pb^{2+} and Pb^0, respectively. The Pb^0/Pb^{tot} atomic ratio is shown in the inset. b) Br/Pb^{tot}, N/Pb^{tot}, and C/Pb^{tot} atomic ratios for the 6 min sputtered $FAPbBr_3$ film. The dashed line indicates Br/Pb^{tot} in $PbBr_2$. c) Same as (b) with reference to Pb^{2+}.

similar to the non-irradiated regions of the sample. It is straightforward to conclude that the degradation of $FAPbBr_3$ begins in the oval S at an intermediate stage between the cases depicted in Figure 2c,d.

The PL data reported above allow us to estimate the threshold values for degradation and self-healing of $FAPbBr_3$, in terms of X-ray areal density. Within ovals C, the photon flux is 7.6×10^9 ph s^{-1} (this values is obtained by normalizing 99% of the total photon flux to the ratio between the area of oval C and the area of the synchrotron spot) and the average photon flux density is 1.3×10^5 ph $(s \times \mu m^2)^{-1}$. Hence, the average photon densities in C for 1 and 10 min irradiation are 7.8×10^6 and 7.8×10^7 ph μm^{-2}, respectively. An intermediate value of 3.9×10^7 ph μm^{-2} can be considered as the threshold for the observation of the self-healing process by PL. By repeating the calculation of the photon density for ovals S (we assume they receive about 0.1% of the photon flux of ovals C), we find 3.9×10^4 ph μm^{-2} to be the threshold value for the observation of degraded $FAPbBr_3$ by PL. Notably, the very low photon density in ovals S does not allow to collect XPS data for characterizing the chemistry of the initial degradation stage of the film.

The combination of XPS and PL analysis provides the following picture. The primary effect of X-rays is the degradation of $FAPbBr_3$ according to reactions (1) and (2) that is observed by PL for X-ray density higher than 3.9×10^4 ph μm^{-2}. An irradiation level higher than 3.9×10^7 ph μm^{-2} leads to the observation of self-healing processes inside the material through enhanced ion migration of FA^+ and Br^-.[28,29] The recovery can be complete in the bulk of the $FAPbBr_3$ films, where gaseous Br_2 is captured as a reagent and reforms the perovskite via the inverse of reactions (1) and (2).[14,18] This process is disfavored on the Br-deficient surface. However, in the presence of ion migration, a recovery pathway for the surface is provided by reaction (5). Experimental data showing explicitly the migration of FA^+ and Br^- ions under soft X-ray irradiation will be reported in the next section.

2.2. Irradiation of Sputtered $FAPbBr_3$ Films

The analysis of chemical reactions occurring at the surface of pristine $FAPbBr_3$ films is complemented with XPS data acquired on Ar^+ ion sputtered films. The sputtering cycles consist of exposing the samples to an ion flux density of 10^5 $Ar^+/(s \times \mu m^2)$ for 3, 6, 9, and 18 min. Sputtering induces evident changes in the surface composition of the films. Surface contaminants are removed efficiently, as testified by the absence of the O 1s peak (Figure S3, Supporting Information). The clean surface displays a visible increase of the Pb and Br signals already after the first sputtering cycle (Figure S4, Supporting Information).

The XPS analysis of the 6 min sputtered film is reported in **Figure 3**. Similar results are obtained for all sputtering times (Figure S5, Supporting Information). The spectra are acquired at 14 min intervals with the soft X-ray beam on the same position, following the acquisition protocols used for the pristine $FAPbBr_3$ films. Figure 3a shows the evolution of the Pb $4f_{7/2}$ lines as a function of the irradiation time. The shift of the peak toward higher binding energy is assigned again to Fermi level pinning by the accumulation of Pb^0 clusters (similar shift for the other core level lines of the material are displayed in Figure S6, Supporting Information). These clusters gives rise to characteristic defect states within the gap of $FAPbBr_3$, whose intensity increases as a function of the sputtering time (Figure S7, Supporting Information).

The Pb^0/Pb^{tot} ratio (inset of Figure 3a) is much higher than in the pristine case. Figure 3b indicates that Br, N, and C are severely understoichiometric just after sputtering. This is expected, since N and C are light elements and gaseous Br_2 produced by sputtering escapes easily from the film surface, while heavy Pb is difficult to sputter away. Initially, the conversion of Pb^{2+} into Pb^0 is weakly contrasted by the re-oxidation of Pb^0, due to the low concentration of FA^+ at the surface. However, for longer exposure times the concentration of N and C increases considerably, especially if compared to Pb^{2+} (Figure 3c). This behavior is a direct signature of the migration of FA^+ from the bulk to the surface. The higher surface content of FA^+ slows down the conversion rate of Pb^{2+} into Pb^0. Notably, for 70 min irradiation N/Pb^{2+} and C/Pb^{2+} are similar to the average values of N/Pb^{tot} and C/Pb^{tot} in Figure 2b. This observation strengthens the hypothesis that the equilibrium surface concentration of FA^+ is determined by vacuum degassing. Finally, Figure 3b shows that Br/Pb^{tot} remains nearly constant (and Br/Pb^{2+} increases, Figure 3c) during irradiation, while $PbBr_2$ is degraded through reaction (2). Since gaseous Br_2 produced by this reaction is lost to vacuum, the nearly constant Br/Pb^{tot} value indicates the migration of Br^- ions from the bulk to the surface of the $FAPbBr_3$ film.

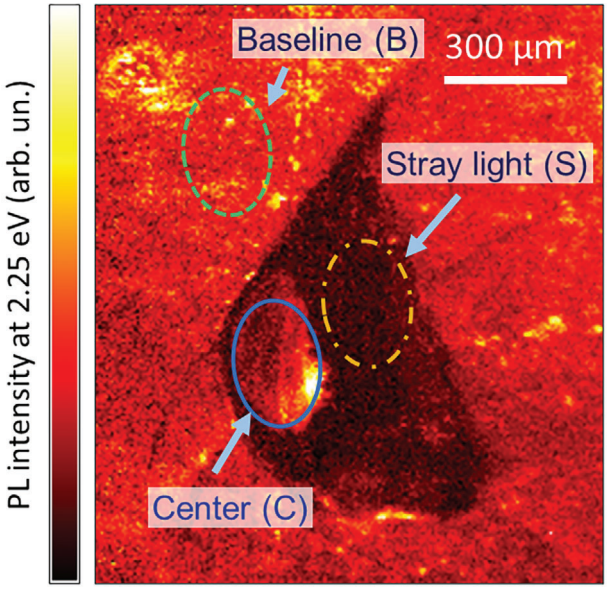

Figure 4. PL map at 2.25 eV after 6 min of sputtering and 60 min of irradiation. B, C, and S areas are highlighted.

The surface chemical analysis reported above is coupled to PL imaging to probe the effects of beam exposure also in the bulk of the material. In general, sputtered samples show lower PL emission compared to the pristine ones, due to the increased density of recombination centers generated by ion sputtering (Figure S8, Supporting Information). After exposing the 6 min sputtered film to synchrotron radiation for 60 min (**Figure 4**; Figure S9, Supporting Information), the signature of degradation (oval S) and self-healing (oval C) are observed by PL, in analogy to the behavior reported in Section 2.1.

XPS and PL observation together hint again at the importance of reaction (5) for the recovery of $FAPbBr_3$ in the case of a Pb^0 rich environment, such as the surface of the film, where the inverse of reactions (1) and (2) are not viable.

2.3. Quantitative PL Analysis of $FAPbBr_3$ Films

To evaluate quantitatively the changes in the optoelectronic properties of the $FAPbBr_3$ films under different conditions of irradiation and sputtering, the PL spectra are fitted by using a model based on Planck's law, which allows to extract Quasi-Fermi Level Splitting (QFLS, Δμ) and energy gap (E_g) of the material.[59,60] **Figure 5**a compares the values of QFLS for the B, C and S areas of the pristine and 6 min sputtered samples exposed to the synchrotron beam for 60 min. Sputtering alone causes a reduction of the QFLS from 1.79 to 1.74 eV. For low photon densities (S areas) the decrease of QFLS is sizeable in both samples. Meanwhile, the irradiation-stimulated recovery in C areas increases the QFLS to values comparable to those measured on the B areas of both samples.

The different stresses have an influence also on the bandgap of the material. The B areas exhibit a bandgap of 2.29 eV for both pristine and sputtered samples, in line with values reported in the literature.[40] Irradiation leads to a slight red-shift of the band gap value in the S (low photon density) areas followed by a blue-shift in C (high photon density) areas. A quantitative indicator of the non-radiative losses of a semiconductor material is the difference $L = E_g - \Delta\mu$, which is reported in Figure S10 (Supporting Information). This analysis reveals that overall the sputtering damages the material, as L increases from 0.5 to 0.55 eV. In any case, after prolonged irradiation the losses in the C areas are negligible if compared to the values in the B areas.

3. Conclusion

The combination of XPS analysis, which provides chemical sensitivity, and PL imaging at the micro-scale[57,58] allows to obtain a comprehensive picture of the processes occurring in $FAPbBr_3$ under soft X-rays (**Figure 6**). For photon density lower than 3.9×10^4 ph μm^{-2} there is no evidence of changes in the optoelectronic properties of the pristine material (Figure 6a). The decomposition of $FAPbBr_3$, driven by reactions (1) and (2), prevails for photon density between 3.9×10^4 and 3.9×10^7 ph μm^{-2} (Figure 6b). This is accompanied by a decrease in PL emission compared to the non-irradiated material and the formation of Pb^0 metallic clusters. Photon densities higher than 3.9×10^7 ph μm^{-2} (Figure 6c) stimulate self-healing of the material, which occurs through re-oxidation of Pb^0 and enhanced ion migration, as directly observed by XPS. The self-healing process is able to restore completely the optoelectronic properties of $FAPbBr_3$ in the bulk, where the degradation products remain trapped. Instead, the full recovery is disfavored on the surface due to the loss of gaseous Br_2.

The self-healing of $FAPbBr_3$ stimulated by X-ray exposure is reported for the first time in the present study. The experimental observations and the proposed chemical paths for the degradation and restoring of the optoelectronic properties provide a complementary perspective to previous studies exploring the interaction of $FAPbBr_3$ with lower energy light. From the technological point of view, the results suggest that $FAPbBr_3$ films could be exploited as light adsorbers in X-ray detectors operating in high-dose environments.

4. Experimental Section

Sample Preparation: $FAPbBr_3$ solution (1.3 M) was prepared starting from stoichiometric concentrations of $PbBr_2$ and FABr powder precursors in DMSO solvent. The $FAPbBr_3$ perovskite films were deposited by spin-coating on FTO/c-TiO_2 substrates (FTO/c-TiO_2/$FAPbBr_3$) at 4000 rpm for 20 s using the solvent quenching method. After 10 s, 200 µl of ethylacetate antisolvent was dropped above the samples. Then, the samples were annealed at 80 °C for 10 min to obtain the final $FAPbBr_3$ films.

Material Characterization: XPS measurements were performed at the VUV-Photoemission beamline at Elettra (Trieste, Italy). Core levels were measured with $h\nu = 750$ eV. The acquisition time of a set of O 1s, N 1s, C 1s, Pb 4f, and Br 3d spectra was 14 min. Five sets were acquired consecutively on the pristine and sputtered samples. Valence band spectra shown in Figure S7 (Supporting Information) was collected with $h\nu = 65$ eV. All experiments were performed in ultra-high vacuum conditions (10^{-10} mbar regime) at the temperature of 20 °C.

Core levels were fitted with Voigt functions.[61] The atomic ratios of element x with respect to element y were determined as:

$$\frac{A_x/\sigma_x}{A_y/\sigma_y} \quad (6)$$

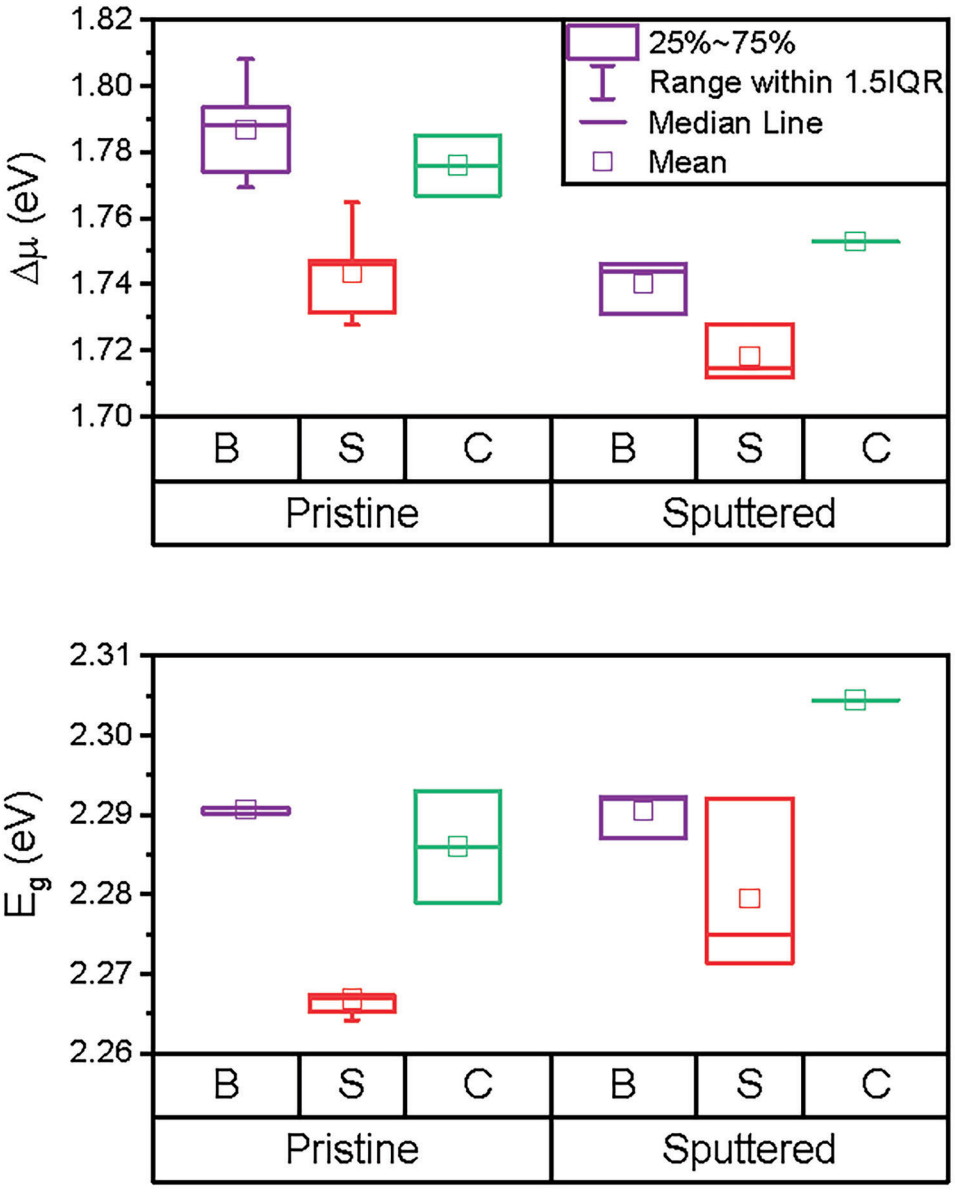

Figure 5. a) Quasi-Fermi level splitting Δμ and b) energy gap E_g values calculated from the PL spectra collected in the B, S, and C areas of pristine and 6 min sputtered samples after 60 min X-ray exposure.

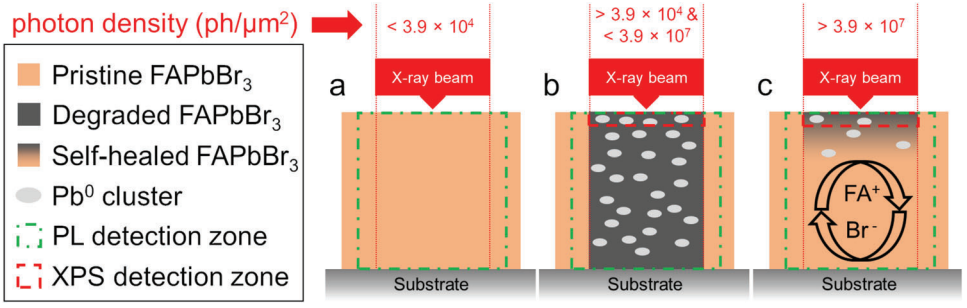

Figure 6. Sketch of the degradation/self-healing process in $FAPbBr_3$ under soft X-rays. a) Below 3.9×10^4 ph μm^{-1} no change in the optoelectronic properties of the material is observed. b) For photon densities between 3.9×10^4 and 3.9×10^7 ph μm^{-2} the PL signal shows a drop and metallic Pb^0 clusters are detected. c) Higher photon densities favor the re-oxidation of Pb^0 and stimulate the migration of mobile FA^+ and Br^- ions, which participate in the recovery of the material properties.

where the core levels areas A_x and A_y were normalized to the corresponding photoemission cross sections σ_x and σ_y at $h\nu = 750$ eV.[62]

Photoluminescence Imaging: The hyperspectral imaging system records a luminescence intensity signal along three dimensions (x, y, λ). The set-up was composed by a home-built microscope with Thorlabs optomechanical elements, a 2D bandpass filtering system from company Photon Etc with 2 nm resolution, and a 1 Mpix silicon-based CCD camera PCO1300. The samples were illuminated with a LED (λ= 405 nm) through an infinity-corrected × 4 Olympus objective with numerical aperture of 0.10, and the luminescence was collected through the same objective. The beam size of the 405 nm LED was larger than 5 mm and the illumination was homogenous over the sample. The incident photon flux was 0.45 mW cm^{-2}. The excitation beam and luminescence signals were separated with appropriate Thorlabs dichroic beam splitter (DMLP425R) and filters (FELH 0450). The 2D luminescence signal was corrected for each pixel of the sensor from the spectral transmissions along all the optical path, from the read noise and dark current noise of the camera. Samples were exposed to ambient conditions for a few days between X-ray exposure and PL measurements. All acquisitions were performed in nitrogen atmosphere at the temperature of 20 °C. Post-treatment of the data cubes includes a deconvolution and fit to the generalized Planck law. The latter is described in Section S1 (Supporting Information).

Supporting Information

Supporting Information is available from the Wiley Online Library or from the author.

Acknowledgements

The authors acknowledge the European Project "Energy Harvesting in Cities with Transparent and Highly Efficient Window-Integrated Multi-Junction Solar Cells" (CITYSOLAR) for supporting the work, which received funding from the European Union's Horizon2020 research and innovation program under grant agreement number 101007084. D.R.C. thanks the European Union's Horizon 2020 research and innovation program under the Marie Sklodowska-Curie grant agreement no. 893194. P.S. thanks the French Agence Nationale de la Recherche for funding under the contract number ANR-17-MPGA-0012. P.M.S. and P.M. acknowledge the project EUROFEL-ROADMAP ESFRI of the Italian Ministry of Education, University, and Research.

Conflict of Interest

The authors declare no conflict of interest.

Data Availability Statement

The data that support the findings of this study are available from the corresponding author upon reasonable request.

Keywords

perovskites, photoemission spectroscopy, photoluminescence imaging, self-healing, soft X-rays

Received: February 21, 2023
Revised: May 8, 2023
Published online: June 7, 2023

[1] P. S. Schulze, K. Wienands, A. J. Bett, S. Rafizadeh, L. E. Mundt, L. Cojocaru, M. Hermle, S. W. Glunz, H. Hillebrecht, J. C. Goldschmidt, *Thin Solid Films* **2020**, *704*, 137970.
[2] B. Dridi Rezgui, I. Touhami, F. Khan, K. Ben Messaoud, C. Ben Alaya, Z. Antar, M. Bouaïcha, *Opt. Mater.* **2023**, *135*, 113267.
[3] L. Schmidt-Mende, V. Dyakonov, S. Olthof, F. Ünlü, K. M. T. Lê, S. Mathur, A. D. Karabanov, D. C. Lupascu, L. M. Herz, A. Hinderhofer, F. Schreiber, A. Chernikov, D. A. Egger, O. Shargaieva, C. Cocchi, E. Unger, M. Saliba, M. M. Byranvand, M. Kroll, F. Nehm, K. Leo, A. Redinger, J. Höcker, T. Kirchartz, J. Warby, E. Gutierrez-Partida, D. Neher, M. Stolterfoht, U. Würfel, M. Unmüssig, et al., *APL Materials* **2021**, *9*, 109202.
[4] J. J. Yoo, S. S. Shin, J. Seo, *ACS Energy Lett.* **2022**, *7*, 2084.
[5] J. Jeong, M. Kim, J. Seo, H. Lu, P. Ahlawat, A. Mishra, Y. Yang, M. A. Hope, F. T. Eickemeyer, M. Kim, Y. J. Yoon, I. W. Choi, B. P. Darwich, S. J. Choi, Y. Jo, J. H. Lee, B. Walker, S. M. Zakeeruddin, L. Emsley, U. Rothlisberger, A. Hagfeldt, D. S. Kim, M. Grätzel, J. Y. Kim, *Nature* **2021**, *592*, 381.
[6] G. Li, Z. Su, L. Canil, D. Hughes, M. H. Aldamasy, J. Dagar, S. Trofimov, L. Wang, W. Zuo, J. J. Jerónimo-Rendon, M. M. Byranvand, C. Wang, R. Zhu, Z. Zhang, F. Yang, G. Nasti, B. Naydenov, W. C. Tsoi, Z. Li, X. Gao, Z. Wang, Y. Jia, E. Unger, M. Saliba, M. Li, A. Abate, *Science* **2023**, *379*, 399.
[7] Z. Pan, L. Wu, J. Jiang, L. Shen, K. Yao, *J. Phys. Chem. Lett.* **2022**, *13*, 2851.
[8] A. Glushkova, P. Andričević, R. Smajda, B. Náfrádi, M. Kollár, V. Djokić, A. Arakcheeva, L. Forró, R. Pugin, E. Horváth, *ACS Nano* **2021**, *15*, 4077.
[9] M. Yao, J. Jiang, D. Xin, Y. Ma, W. Wei, X. Zheng, L. Shen, *Nano Lett.* **2021**, *21*, 3947.
[10] Q. A. Akkerman, L. Manna, *ACS Energy Lett.* **2020**, *5*, 604.
[11] B. P. Finkenauer, Akriti, K. Ma, L. Dou, *ACS Appl. Mater. Interfaces* **2022**, *14*, 24073.
[12] D. Cahen, L. Kronik, G. Hodes, *ACS Energy Lett.* **2021**, *6*, 4108.
[13] M. D. Keersmaecker, N. R. Armstrong, E. L. Ratcliff, *Energy Environ. Sci* **2021**, *14*, 4840.
[14] D. R. Ceratti, Y. Rakita, L. Cremonesi, R. Tenne, V. Kalchenko, M. Elbaum, D. Oron, M. A. C. Potenza, G. Hodes, D. Cahen, *Adv. Mater.* **2018**, *30*, 1706273.
[15] L. Shi, M. P. Bucknall, T. L. Young, M. Zhang, L. Hu, J. Bing, D. S. Lee, J. Kim, T. Wu, N. Takamure, D. R. McKenzie, S. Huang, M. A. Green, A. W. Y. Ho-Baillie, *Science* **2020**, *368*, 6497.
[16] D. R. Ceratti, A. V. Cohen, R. Tenne, Y. Rakita, L. Snarski, N. P. Jasti, L. Cremonesi, R. Cohen, M. Weitman, I. Rosenhek-Goldian, I. Kaplan-Ashiri, T. Bendikov, V. Kalchenko, M. Elbaum, M. A. C. Potenza, L. Kronik, G. Hodes, D. Cahen, *Mater. Horiz.* **2021**, *8*, 1570.
[17] S. Aharon, D. R. Ceratti, N. P. Jasti, L. Cremonesi, Y. Feldman, M. A. C. Potenza, G. Hodes, D. Cahen, *Adv. Funct. Mater.* **2022**, *32*, 2113354.
[18] D. R. Ceratti, R. Tenne, A. Bartezzaghi, L. Cremonesi, L. Segev, V. Kalchenko, D. Oron, M. A. C. Potenza, G. Hodes, D. Cahen, *Adv. Mater.* **2022**, 2110239.
[19] A. Senocrate, G. Y. Kim, M. Grä1tzel, J. Maier, *ACS Energy Lett.* **2019**, *4*, 2859.
[20] T. Buffeteau, L. Hirsch, D. M. Bassani, *Adv. Mater.* **2021**, *33*, 2007715.
[21] D. R. Ceratti, A. Zohar, R. Kozlov, H. Dong, G. Uraltsev, O. Girshevitz, I. Pinkas, L. Avram, G. Hodes, D. Cahen, *Adv. Mater.* **2020**, *32*, 2002467.
[22] D. R. Ceratti, A. Zohar, G. Hodes, D. Cahen, *Adv. Mater.* **2021**, *33*, 2102822.
[23] Y. Yuan, J. Huang, *Acc. Chem. Res.* **2016**, *49*, 286.
[24] R. A. Scheidt, P. V. Kamat, *J. Chem. Phys.* **2019**, *151*, 134703.
[25] Y. Yuan, Q. Wang, Y. Shao, H. Lu, T. Li, A. Gruverman, J. Huang, *Adv. Energy Mater.* **2015**, *6*, 1501803.
[26] Y. Yuan, J. Chae, Y. Shao, Q. Wang, Z. Xiao, A. Centrone, J. Huang, *Adv. Energy Mater.* **2015**, *5*, 1500615.
[27] A. Urbaniak, A. Czudek, J. Dagar, E. Unger, *Sol. Energy Mater. Sol. Cells* **2022**, *238*, 111618.

[28] A. Oranskaia, J. Yin, O. M. Bakr, J.-L. Brédas, O. F. Mohammed, *J. Phys. Chem. Lett.* **2018**, *9*, 5474.
[29] W. Zhu, S. Wang, X. Zhang, A. Wang, C. Wu, F. Hao, *Small* **2022**, *18*, 2105783.
[30] J. A. Schwenzer, T. Hellmann, B. A. Nejand, H. Hu, T. Abzieher, F. Schackmar, I. M. Hossain, P. Fassl, T. Mayer, W. Jaegermann, U. Lemmer, U. W. Paetzold, *ACS Appl. Mater. Interfaces* **2021**, *13*, 15292.
[31] I. S. Zhidkov, D. W. Boukhvalov, A. F. Akbulatov, L. A. Frolova, L. D. Finkelstein, A. I. Kukharenko, S. O. Cholakh, C.-C. Chueh, P. A. Troshin, E. Z. Kurmaev, *Nano Energy* **2021**, *79*, 105421.
[32] E. S. Vasileiadou, I. Hadar, M. Kepenekian, J. Even, Q. Tu, C. D. Malliakas, D. Friedrich, I. Spanopoulos, J. M. Hoffman, V. P. Dravid, M. G. Kanatzidis, *Chem. Mater.* **2021**, *33*, 5085.
[33] A. F. Akbulatov, V. M. Martynenko, L. A. Frolova, N. N. Dremova, I. Zhidkov, S. A. Tsarev, S. Y. Luchkin, E. Z. Kurmaev, S. M. Aldoshin, K. J. Stevenson, P. A. Troshin, *Sol. Energy Mater. Sol. Cells* **2020**, *213*, 110559.
[34] P. Raval, R. M. Kennard, E. S. Vasileiadou, C. J. Dahlman, I. Spanopoulos, M. L. Chabinyc, M. Kanatzidis, G. N. M. Reddy, *ACS Energy Lett.* **2022**, *7*, 1534.
[35] E. J. Juarez-Perez, L. K. Ono, Y. Qi, *J. Mater. Chem. A* **2019**, *7*, 16912.
[36] N. Arora, M. I. Dar, M. Abdi-Jalebi, F. Giordano, N. Pellet, G. Jacopin, R. H. Friend, S. M. Zakeeruddin, M. Grätzel, *Nano Lett.* **2016**, *16*, 7155.
[37] Y. Liu, B. J. Kim, H. Wu, L. Yuan, H. Zhu, A. Liu, E. M. J. Johansson, *ACS Appl. Energy Mater.* **2020**, *3*, 9817.
[38] Y. Liu, B. J. Kim, H. Wu, G. Boschloo, E. M. J. Johansson, *ACS Appl. Energy Mater.* **2021**, *4*, 9276.
[39] M. A. der Maur, F. Matteocci, A. D. Carlo, M. Testa, *Appl. Phys. Lett.* **2022**, *120*, 113505.
[40] G. Mannino, I. Deretzis, E. Smecca, A. L. Magna, A. Alberti, D. Ceratti, D. Cahen, *J. Phys. Chem. Lett.* **2020**, *11*, 2490.
[41] F. Matteocci, D. Rossi, L. A. Castriotta, D. Ory, S. Mejaouri, M. A. der Maur, F. Sauvage, S. Cacovich, A. D. Carlo, *Nano Energy* **2022**, *101*, 107560.
[42] H. Chen, L. Fan, R. Zhang, C. Bao, H. Zhao, W. Xiang, W. Liu, G. Niu, R. Guo, L. Zhang, L. Wang, *Adv. Opt. Mater.* **2020**, *8*, 1901390.
[43] H. Wu, Y. Ge, G. Niu, J. Tang, *Matter* **2021**, *4*, 144.
[44] A. W. Y. Ho-Baillie, H. G. J. Sullivan, T. A. Bannerman, H. P. Talathi, J. Bing, S. Tang, A. Xu, D. Bhattacharyya, I. H. Cairns, D. R. McKenzie, *Adv. Mater. Technol.* **2021**, *7*, 2101059.
[45] D. P. del Rey, C. Dreessen, A. M. Igual-Muñoz, L. van den Hengel, M. C. Gélvez-Rueda, T. J. Savenije, F. C. Grozema, C. Zimmermann, H. J. Bolink, *Sol. RRL* **2020**, *4*, 2000447.
[46] J. Yang, Q. Bao, L. Shen, L. Ding, *Nano Energy* **2020**, *76*, 105019.
[47] J. Pang, S. Zhao, X. Du, H. Wu, G. Niu, J. Tang, *Light: Sci. Appl.* **2022**, *11*, 1.
[48] J. Barichello, D. D. Girolamo, E. Nonni, B. Paci, A. Generosi, M. Kim, A. Levtchenko, S. Cacovich, A. D. Carlo, F. Matteocci, *Sol. RRL* **2022**, *7*, 2200739.
[49] S. Thampy, B. Zhang, J.-G. Park, K.-H. Hong, J. W. P. Hsu, *Mater. Adv.* **2020**, *1*, 3349.
[50] Y. Li, X. Xu, C. Wang, B. Ecker, J. Yang, J. Huang, Y. Gao, *J. Phys. Chem. C* **2017**, *121*, 3904.
[51] A. Alberti, C. Bongiorno, E. Smecca, I. Deretzis, A. L. Magna, C. Spinella, *Nat. Commun.* **2019**, *10*, 1.
[52] M. R. Tubbs, A. J. Forty, *Br. J. Appl. Phys.* **1964**, *15*, 1553.
[53] P. W. Wang, J.-C. Hsu, L.-G. Hwa, *J. Non-Cryst. Solids* **2008**, *354*, 1256.
[54] F.-S. Zu, P. Amsalem, I. Salzmann, R.-B. Wang, M. Ralaiarisoa, S. Kowarik, S. Duhm, N. Koch, *Adv. Opt. Mater.* **2017**, *5*, 1700139.
[55] R. A. Kerner, P. Schulz, J. A. Christians, S. P. Dunfield, B. Dou, L. Zhao, G. Teeter, J. J. Berry, B. P. Rand, *APL Mater.* **2019**, *7*, 041103.
[56] A. Singh, F. Matteocci, H. Zhu, D. Rossi, S. Mejaouri, S. Cacovich, M. A. D. Maur, F. Sauvage, A. Gagliardi, M. Grätzel, A. D. Carlo, *Sol. RRL* **2021**, *5*, 2100277.
[57] S. Cacovich, P. Dally, G. Vidon, M. Legrand, S. Gbegnon, J. Rousset, J.-B. Puel, J.-F. Guillemoles, P. Schulz, M. Bouttemy, A. Etcheberry, *ACS Appl. Mater. Interfaces* **2022**, *14*, 34228.
[58] S. Cacovich, D. Messou, A. Bercegol, S. Béchu, A. Yaiche, H. Shafique, J. Rousset, P. Schulz, M. Bouttemy, L. Lombez, *ACS Appl. Mater. Interfaces* **2020**, *12*, 34784.
[59] J. K. Katahara, H. W. Hillhouse, *J. Appl. Phys.* **2014**, *116*, 173504.
[60] N. Paul, V. L. Guen, D. Ory, L. Lombez, in *2017 IEEE 44th Photovoltaic Specialist Conference (PVSC)*, IEEE, Washington DC, USA **2017**.
[61] M. Wojdyr, *J. Appl. Crystallogr.* **2010**, *43*, 1126.
[62] J.-J. Yeh, in *Atomic Calculation of Photoionization Cross-Selections and Asymmetry Parameters*, Gordon and Brach Science Publishers, Philadelphia, PE, USA **1993**.

